Accepted version published in: *J. Roy. Soc. Interface*, 17, 20200239 (2020)

Biomimicry of iridescent, patterned insect cuticles: comparison of biological and synthetic, cholesteric microcells using hyperspectral imaging

Aurélie Jullien[*,†], Maxim Neradovskiy[†], Adriana Scarangella[‡] and Michel Mitov[*,‡]

†Institut de Physique de Nice, Université Côte d'Azur, CNRS, UMR 7010, Valbonne, France

‡Centre d'Elaboration de Matériaux et d'Etudes Structurales, CEMES, CNRS, UPR 8011, Université de Toulouse, Toulouse, France

AJ, 0000-0002-7776-8312; MM, 0000-0003-1831-2152

Biological systems inspire the design of multifunctional materials and devices. However, current synthetic replicas rarely capture the range of structural complexity observed in natural materials. Prior to the definition of a biomimetic design, a dual investigation with a common set of criteria for comparing the biological material and the replica is required. Here, we deal with this issue by addressing the non-trivial case of insect cuticles tessellated with polygonal microcells with iridescent colors due to the twisted cholesteric organization of chitin fibers. By using hyperspectral imaging within a common methodology, we compare, at several length scales, the textural, structural and spectral properties of the microcells found in the two-band cuticle of the scarab beetle *Chrysina gloriosa* with those of the polygonal texture formed in flat films of cholesteric liquid crystal oligomers. The hyperspectral imaging technique offers

a unique opportunity to reveal the common features and differences in the spectral-spatial signatures of biological and synthetic samples at a 6-nm spectral resolution over 400 nm-1000 nm and a spatial resolution of 150 nm. The biomimetic design of chiral tessellations is relevant to the field of non-specular properties such as deflection and lensing in geometric phase planar optics.

Research paper

Cite this article: Jullien A, Neradovskiy M, Scarangella A, Mitov M., 2020, Biomimicry of iridescent, patterned insect cuticles: comparison of biological and synthetic, cholesteric microcells using hyperspectral imaging. *J. R. Soc. Interface* 17: 20200239

http://dx.doi.org/10.1098/rsif.2020.0239

Received: 8 April 2020

Accepted: 27 May 2020

Subject Category: Life Sciences-Physics interface

Subject Areas: biophysics, biomimetics

Keywords: insect cuticle, chitin, cholesteric, biomimetics, biophotonics, optical imaging

***Authors for correspondence:**

Aurélie Jullien

e-mail: aurelie.jullien@inphyni.cnrs.fr

Michel Mitov

e-mail: mitov@cemes.fr

Accepted version published in: *J. Roy. Soc. Interface*, 17, 20200239 (2020)

1 Introduction

1.1 Motivation of the research

A wide diversity of patterns and colors is found in nature and at different length scales.[1,2] Biological systems inspire the design of novel optical materials for addressing modern challenges in bioengineering, energy capture and conversion, sensing, communication, light shaping or data processing.[3] However, current replicas rarely capture the range of structural complexity observed in natural materials, as acknowledged in recent reviews.[3–5] In particular, the biomimetic design of insect cuticles is in its infancy because the design tools necessary for the control of nano- and microscale patterns with a high level of versatility are pending.[6]

The iridescent structural colors of insect cuticles are in most cases due to the twisted cholesteric liquid crystal (CLC) organization of the chitin fibers.[7,8] Chitin macromolecules form fibrils that wrap with proteins and assemble into fibers, which assemble into bundles. The bundles arrange themselves parallel to each other and form pseudo-layers. Finally, the chitin fiber-protein pseudo-layers stack into a twisted plywood Bouligand structure with the pseudo-layers rotated around the normal axis of the cuticle[9] (Fig. 1a). Although the stripe fingerprint texture as seen in cross-sectional views (Fig. 1e) gives the appearance of a layered system, the twisted plywood (cholesteric) structure is not a discrete multilayer system: a continuous twist occurs along the axis perpendicular to the fibres, which interpenetrate from pseudo-layer to pseudo-layer. For this reason, we use the term pseudo-layer in place of layer. A 360° rotation of the fiber orientation defines the helical pitch. Bragg reflections occur when the helical pitch is on the order of the wavelength of the incident light[10]. For circularly polarized light propagating along the helical axis

with the same handedness as the helix, a CLC exhibits a reflection band over the wavelength range of $(n_o\text{-}n_e)p$, where n_o and n_e are the ordinary and extraordinary refractive indices of the material and p is the helical pitch.

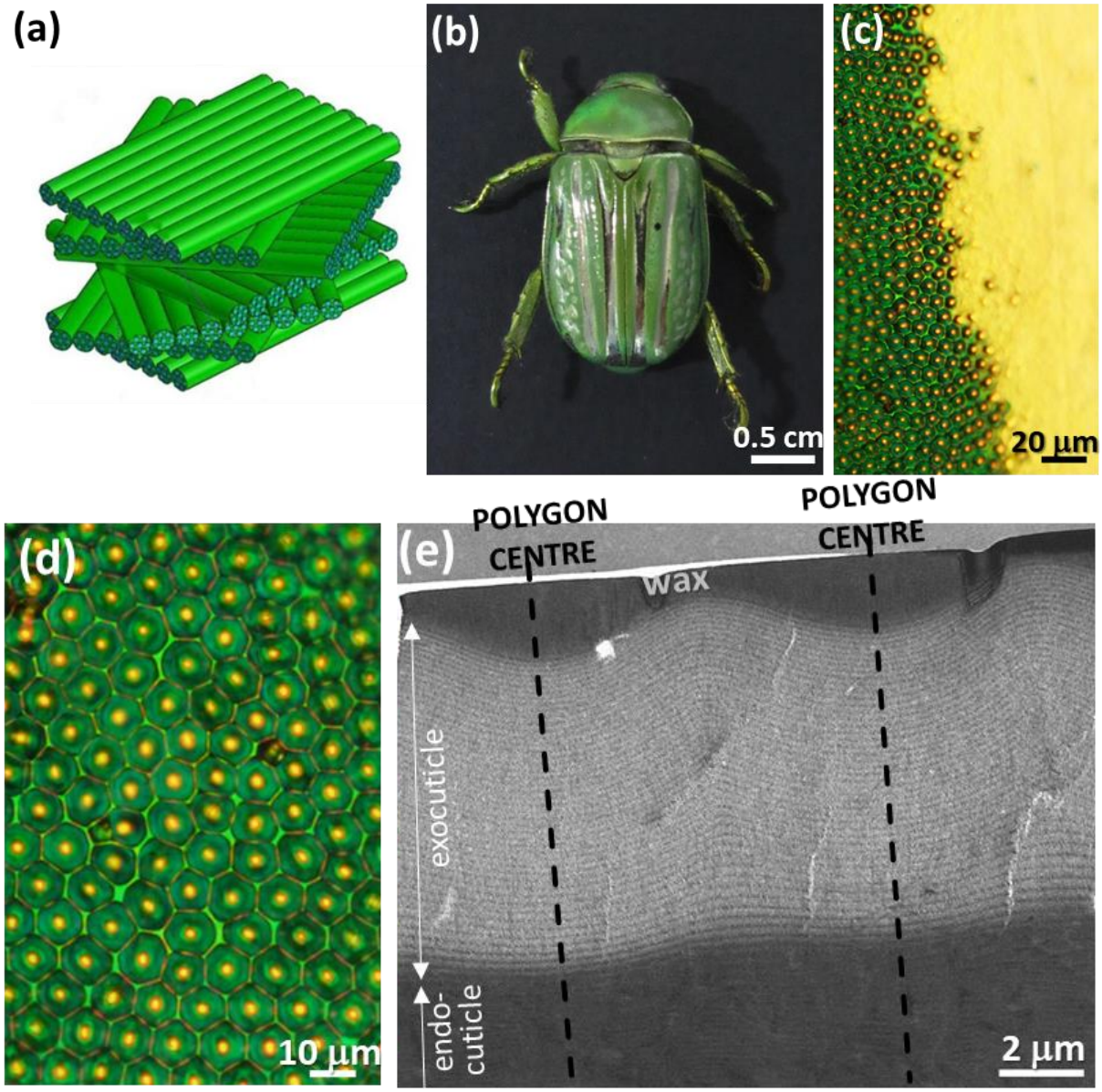

Figure 1: (a) The twisted plywood structure of chitin fiber-protein pseudo-layers in the insect cuticle (adapted from [60], Creative Commons license). (b) Scarab beetle *Chrysina gloriosa*. (c)

Green and silver bands at the interface as observed by optical microscopy (reflection mode, unpolarized light). (d) Magnified view of the polygonal texture in the green bands. (e) TEM image of the cuticle in the green bands. The location of a couple of polygons is reported. The fingerprint texture appears as a network of dark and bright stripes.

In biomimicry, many of the same species come up: geckos, spiders, and butterflies. [11] Replicas of butterfly wings are dominant in the field of insect photonic structures. The (twist-free) multilayer structure of wing scales is based on alternate air layers and pillar-supported chitinous layers, which leads to optical interference.[12] Many replication methods have been developed on the basis of three concepts that use wing scales as templates: coating, modification and filling. [13] The morphology of the produced materials can be hard to control, and the choice of the method depends on the requirements of the situation.

Biomimetic cuticles of beetles are especially rare because the design solutions are challenging.[14] Investigations aiming at reproducing these biological structures as closely as possible have addressed the case of the untextured cuticle of the gold scarab beetle *Plusiotis resplendens*. Three-layer replicas were fabricated by inserting a nematic LC layer, acting as a half-wave retardation plate, between two left-handed cholesteric layers with a UV-crosslinked elastomer[15], or with chiral cellulose nanocrystals after water evaporation.[16]

To realize biomimicry, reproducing cuticles with fidelity requires a precise comparison of the chiro-optical properties of artificial structures and biological structures. With this objective in mind, here, we address the intriguing case of reflective microcells. Some representative examples can be found in the cuticles of manuka beetles,[17] June beetles,[18] *Plusiotis boucardi*,[19] *Chlorophila*

obscuripennis,[20] several tiger beetles of the genus *Cicindela*,[21,22] *Calidea panaethiopica*,[23] *Chrysochroa fulgidissima*,[24] *Anomala dimidata*[25] or *Chrysina aurora*.[26] The genus *Chrysina* is a large genus of insects that have been widely studied for their vibrant iridescence and polarization properties.[27] Most cuticles of *Chrysina* beetles are green colored or have a metallic gold or silver aspect. The scarab beetle *Chrysina gloriosa* (Fig. 1b), with both green and metallic silver bands (Fig. 1c), is emblematic of the genus *Chrysina*. At the micrometer scale, a cellular polygonal texture can be observed in the green bands (Fig. 1d). Each cell contains a bright yellow core with orange edges surrounded by a dark-green region, with a brighter green rim delimiting the cells. Transmission electron microscopy (TEM) investigations of a cross-section (Fig. 1e) allows imaging of the cholesteric fingerprint (stripe) texture. The distance between two identical stripes is related to the helical half-pitch. A pitch gradient occurs from the top to the bottom of the chitinous part of the cuticle. The stripes are curved below the polygonal cells in the upper part, which means that the orientation of the helical axis is tilted here. The stripes progressively become straight in the rest of the structure (the helical axis stays fixed). The silver bands exhibit a non-patterned planar texture and behave as specular broadband mirrors, from the beginning of the visible spectrum to the infrared spectrum.[28] The last part of the cuticle consists of a wax layer, which, in the insect world, generally speaking, may serve to restrict water loss, prevent desiccation and enable chemical communication.[29] In the absence of information on their internal physical organization, cuticular waxes have been considered isotropic. However, the presence of a nanoscale stripe texture was recently reported for *C. gloriosa*.[30]

1.2 State-of-the-art

Previous studies on the polygonal texture of *C. gloriosa* have reported a cellular structure of concentric rings, as shown by transmission electron microscopy (TEM)[31] or fluorescence confocal microscopy;[32] a low degree of circular polarization, as shown by Mueller matrix spectroscopic ellipsometry;[33] a multiwavelength micromirror nature of the polygonal cells;[28] and the generation of self-healing Bessel beams from the polygonal cells, which may be approached as axicon cells.[34]

In synthetic CLCs, polygonal textures consisting of a mosaic of polygons of various sizes (Fig. 2a) are easily available from flat cholesteric films when the helical axis is tilted with respect to the surfaces of the films. This situation is promoted in an open film via hybrid anchoring of the molecules, which preferentially align tangentially to the solid substrate on which the material is coated and perpendicular to the air interface. The overall question is to what extent these synthetic textures are precisely comparable to the biological assemblies of microcells.

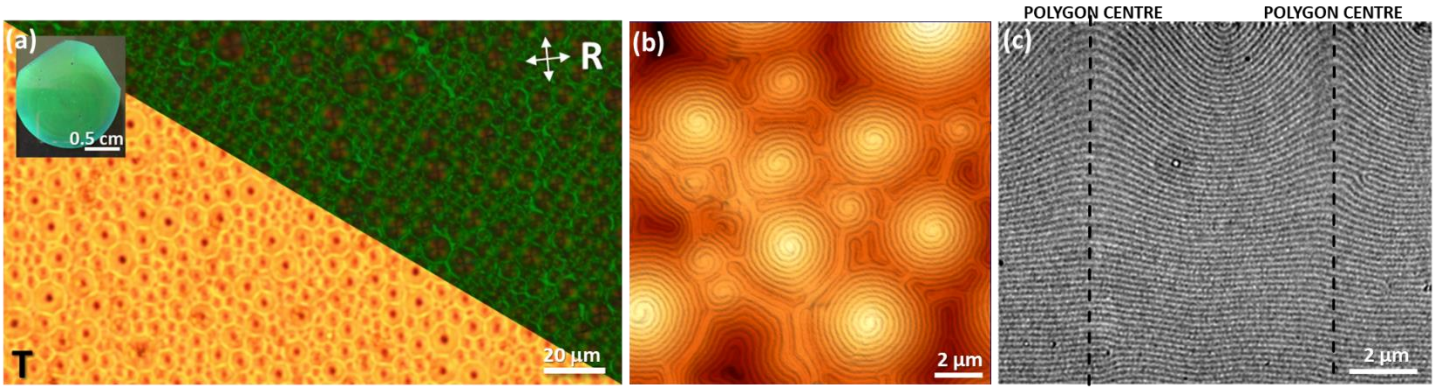

Figure 2: (a) Polygonal cholesteric textures observed in the synthetic material of the present study (sample PG30) by optical microscopy in transmission (unpolarized light) and reflection modes. The white arrows indicate the orientations of the crossed polarizers for the reflection mode. Inset: open film coated on a glass plate. (b) AFM image of the polygonal field at the free

surface of an open film. (c) TEM image of the transverse structure of an open film showing the arc patterns close to the air interface (top) and the straight stripes close to the glass substrate interface (bottom). The location of a couple of polygons is reported.

Most optical and structural investigations on the cholesteric polygonal texture[35–43] have focused on polysiloxane-based oligomers such as those of the present study (Fig. 3). Atomic force microscopy (AFM) reveals a cone shape of the polygonal cells, which are the locus of the double-spiral patterns (Fig. 2b). The relief of the conical polygons (their height is in the 20-100 nm range)[37] results from the competition between the surface energy and the bulk free energy. The surface tension minimizes the surface area by rearranging the fluid interface from a planar state to a polygonal field.[44] The energy is lowered by transforming the free surface into a cone, thus reducing the bulk distortion energy at the cost of the surface energy. The double-spiral patterns correspond to the adaptation of the cholesteric structure to the relief and anchoring conditions at the limits.

Close to air, the twisted structure cannot readily adapt to the anchoring conditions. One solution to this boundary problem is to create a series of alternating disclination lines at the surface[45]. Nested-arc patterns are observed by TEM in cross-sectional views (Fig. 2c); they develop because the anchoring at the free surface favors an oblique orientation of the helical axis relative to the surface.

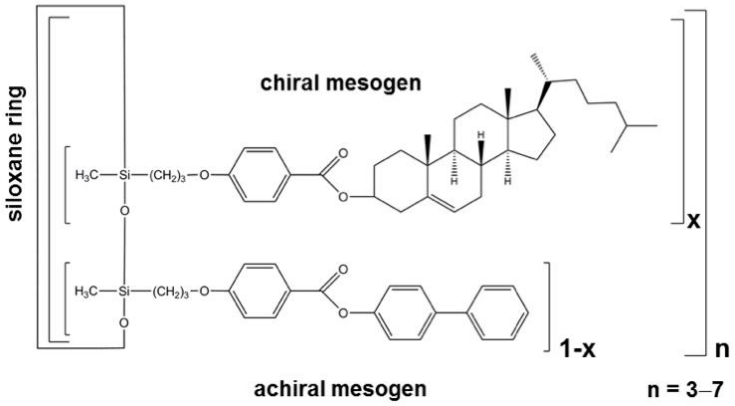

	Green
x = molar percentage of chiral mesogens	44
Bandgap λ_{min}–λ_{max} (nm)	480–560
Glass transition temperature (°C)	45-55
Clearing temperature (°C)	180-210

Figure 3: Liquid crystalline oligomers: general chemical formula and main features of the compound used in the present study.

On the basis of the similarities between the optical textures, it was believed that the polygonal cells of *C. gloriosa* were structurally and optically analogous to the focal conic domains spontaneously formed on the free surface of a CLC film.[32] However, the biological texture exhibits concave cells (Fig. 1e), whereas the artificial texture has convex cells (Fig. 2c), based on scanning electron microscopy (SEM) and TEM investigations of cross-sections and numerical simulations.[28] Here, we use the hyperspectral imaging technique to finely compare the spectral details of biological and synthetic textures by providing a description with a 6-nm-scale spectral resolution over 400 nm-1000 nm and a spatial resolution of 150 nm. We demonstrate that the fine spectral-spatial signature of so-called bioinspired structures is quantitatively distinct from that of biological materials.

2 Materials and Methods

2.1 Samples and their characterization

Scarab beetle. A male specimen of *C. gloriosa* was collected in Saltillo (Coahuila, Mexico) in July 2009.

Oligomers. CLC oligomers from Wacker Chemie GmbH were used.[46] They consist of a siloxane ring to which two types of side chains are attached via aliphatic spacers: an achiral mesogen and a chiral cholesterol-bearing mesogen (Fig. 3). The pitch depends on the molar percentage of chiral mesogens in the molecule. Via chemical engineering, different percentages therefore give rise to different films with a reflection color ranging from blue to red. We chose the green compound for which the mean position of the reflection band is located at 540 nm. The cholesteric structure is left-handed. The ordinary and extraordinary refractive indices were assessed to be $n_o = 1.4$ and $n_e = 1.6$.[47] The cholesteric phase appears between 180-210°C (clearing temperature range) and 45-55°C (glass-transition temperature range). After thermal annealing in the viscous cholesteric phase, the films and their optical properties can be fixed into a glassy solid state by thermal quenching on a metal plate.

Preparation of synthetic films. The films were confined between two glass substrates (plate and cover lamella) separated by spacers with different thicknesses (Table 1). The thickness of films was measured by the interference method based on the wave interference due to the internal reflection between the two inner surfaces of the cell substrates.[48] No surface treatment or alignment

layers were used. The cells were kept in the cholesteric phase at 105°C for 5 minutes. After quenching, the films changed from a viscous state to a glassy solid state. For the removal of the lamella, the samples were kept at low temperature (2°C) for 5 minutes to obtain a smooth interface. The open cells were kept in a viscous state at 140°C for 85 minutes for the formation of the polygonal texture. The films were finally quenched at room temperature.

Sample name	PG6	PG10	PG20	PG30
Thickness (µm)	5.8 ± 0.1	11.0 ± 1.5	21.5 ± 1.5	31.5 ± 1.5

Table 1: Film designation and thickness

Inclusions of biological samples for ultramicrotomy. The cuticle samples corresponded to the elytra and were removed with a razor blade. A small piece of sample was embedded in EMbed812 resin (Electron Microscopy Sciences) that was then cured at 60°C for 48 h.

Preparation of biological samples for TEM by ultramicrotomy. A diamond knife at ambient temperature was used to cut 80-nm-thick ultrathin slices with a Leica UCT ultramicrotome. The material was cut perpendicular to the film surface (cross-sections). Slices were retrieved on single-slot Formvar-coated copper grids (GS21-C3, Gilder Grids Ltd.). The samples were finally stained with UranyLess (brand mixture of lanthanides from Delta microscopy) for 20 minutes and with 3% Reynolds lead citrate (from ChromaLys) for 5 minutes.

Inclusions of synthetic samples for ultramicrotomy. A small piece of material was embedded in EMbed-812 resin that was then cured at 40°C (below the glassy transition temperature of the oligomers) for 6 days.

Preparation of synthetic samples for TEM by ultramicrotomy. A diamond knife at ambient temperature was used to cut 80-nm-thick ultrathin slices with an UltraCut S ultramicrotome from Reichert. The material was cut perpendicular to the film surface (cross-sections). Slices were retrieved on 200 mesh Parlodion-carbon-coated copper grids (Ted Pella, Inc.).

Optical micrographs. Textures were photographed with an Olympus BX51 stereomicroscope equipped with an Olympus DP73 digital camera.

TEM conditions. (a) Synthetic films [thickness = 13.0 (±1.5) µm; annealing time = 18 h]: Philips CM30 microscope operating at 300 kV equipped with a 1024*1024 Gatan CCD camera. (b) Biological samples: Jeol JEM-1400 microscope operating at 80 kV equipped with an 11 MPixels Gatan Orius SC1000B CCD camera.

Atomic force microscopy imaging. A 13.0 (±1.5) µm-thick film (annealing time = 18 h.) was prepared for atomic force microscopy (AFM) imaging of the polygonal texture. AFM measurements were performed at room temperature and under ambient conditions using a Veeco Dimension 3100 Scanning Probe Microscope controlled by a NanoScope 3D controller. The image was obtained in tapping mode.

2.2 Hyperspectral microscopy and data acquisition

Optical setup. Hyperspectral imaging provides an image of a given sample, spectrally resolved with numerous narrow and adjacent spectral bands. In the current experiment, we made use of a formerly described reflective hyperspectral microscope, relying on nematic liquid-crystal-based Fourier spectrometry.[49] The lamp source was a tungsten halogen lamp with a stable spectrum. The

spatial resolution was fixed by the microscope and was 150 nm. The field of view was 16 µm by 64 µm.

Analysis. The principle of the Fourier algorithm is described elsewhere.[49] However, we proposed to implement independent component analysis (ICA) to decrease the noise level and significantly reduce the analysis time.[50]

Outputs. As a result, the instrument output was an image with 512*128 pixels, each of them being spectrally resolved with a 6 nm resolution over 400 nm-1000 nm, that is, a data set of 13.3M points. Extracted results then included the spectral reflectance of a given pixel or cluster of pixels, monochromatic images of the sample (one hundred available between 400 nm and 1000 nm), and finally the typical hyperspectral datacube.

Additional information: All the spectra were normalized with respect to the lamp spectrum. Specific care was taken to ensure the reproducibility and reliability of the results. Hyperspectral films were acquired and analyzed N times for each sample (with $N > 20$).

3 Results and discussion

3.1 Biological versus synthetic samples

3.1.1. Hyperspectral view

Hyperspectral imaging delivers an image of the sample under consideration, with each pixel being spectrally resolved with numerous narrow and adjacent spectral bands.[51,52] Applications of this method cover a wide field of scientific investigations in biological, material and optical sciences:

pulse propagation in diffusive media,[53] fluorescence microscopy[54] or oceanography,[55] to cite a few recent studies. This advanced instrument is thus a powerful tool for the analysis of textures for which the spectral response is conditioned by the spatial organization, as is the case with chiral molecular arrangements.[43,49]

In this section, we compare the hyperspectral response of a cholesteric synthetic sample bearing a polygonal texture with that of the cuticle considered to be similar or analogous to it, namely, the microcells of the green band of *C. gloriosa*. The synthetic sample is referred to as PG30, and more information on its preparation is provided in section 2. It was chosen for this comparison because the mean lateral size of its polygons, approximately 5 µm, is relatively close to that of the beetle microcells (7 µm). In the current experiment, the hyperspectral microscope analyzes the light reflected by the scarab green band and the synthetic sample PG30. They are both illuminated by a non-polarized tungsten halogen lamp. The spectral resolution of the acquisition is 6 nm, while the spatial resolution is 150 nm (see section 2).

Figure 4 presents typical outcomes of the hyperspectral analysis: a selection of monochromatic pictures among the 100 available with our instrument and hyperspectral datacubes featuring the sample in two spatial dimensions and one spectral dimension.

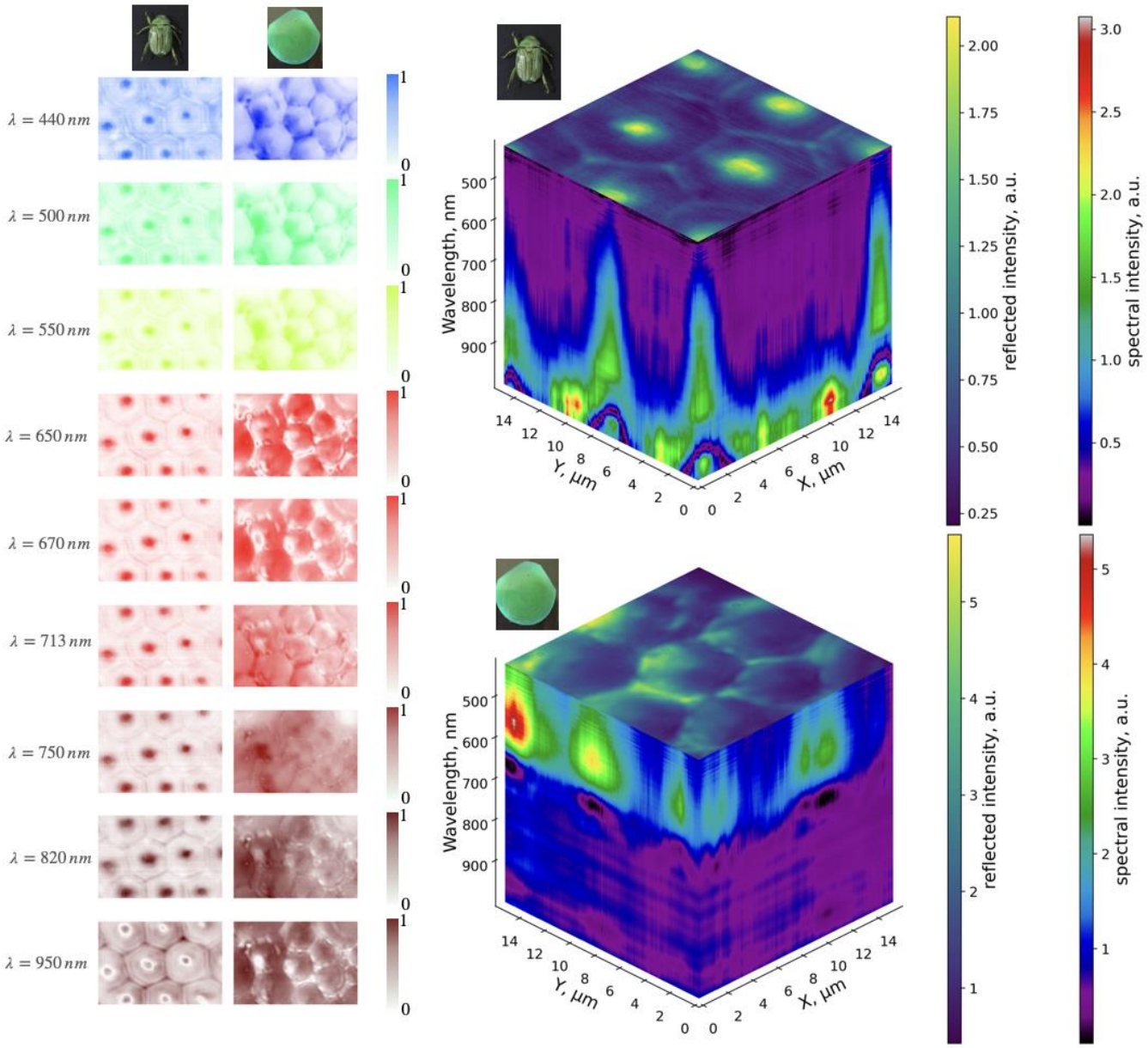

Figure 4: A selection of monochromatic images of the biological sample and synthetic sample *PG*30: each image is normalized (white: 0, dark: 1). Hyperspectral datacubes for both samples. Two different color bars are associated with each cube. The black-to-yellow color bar refers to the overall reflected intensity (i.e., not spectrally resolved), as plotted on the top of the cube (*Y*

versus *X*). The second color bar (black-to-red) refers to the reflected spectral intensity, as plotted on the cube sides (wavelength versus *X*, wavelength versus *Y*).

The monochromatic pictures underline a common feature of the two textures: both act as wavelength-selective elements, with spectral reflectivity differently distributed in the different parts of the microcell (center, lateral part, and valley between cells). These images also illustrate qualitative differences between the two samples, in particular, a reversed bright-dark pattern. The scarab exhibits a regular and structured hexagonal pattern and always shows a bright central point, regardless of the selected wavelength. No bright center spot can be seen for PG, for which the polygon centers are alternately bright or dark depending on the wavelength.

To simultaneously estimate the gradual spectral changes and the spatial modulation of the reflected intensity, the graphic three-dimensional (X, Y, λ) datacube is particularly representative and relevant. A selection of a few polygons is first carried out, with a demarcation line (X=0 and Y=0) passing through valleys and centers of the polygons. The hyperspectral cubes (Fig. 4) then feature the average reflectivity on the top (as a function of X and Y) and the spatially resolved spectral reflectance as lateral maps. Several major differences between the two cubes can be immediately underlined. The beetle presents a broadband reflectivity, between 500 nm and 1000 nm, with a dominant contribution of the hexagon centers. The broad spectral reflectivity of the cuticle is due to the existence of a pitch gradient from the visible to the infrared radiation.[28] Meanwhile, the synthetic sample, having a constant helical pitch across its thickness (Fig. 2c), reflects a narrower bandwidth, enclosed between 450 nm and 650 nm. Furthermore, unlike the cuticle, the valleys are brighter than the centers. The non-overlapping spectral reflection bands and

the different spatial-spectral patterns indicate a structural discrepancy for the axially varying effective pitch of both samples.

3.1.2. Disjoint reflected spectral bandwidths and inverse curvature of the helical structure

To go further, we first present some typical spectra, reflected by a center or valley of the structure, for the two samples under study (Fig. 5a, b).

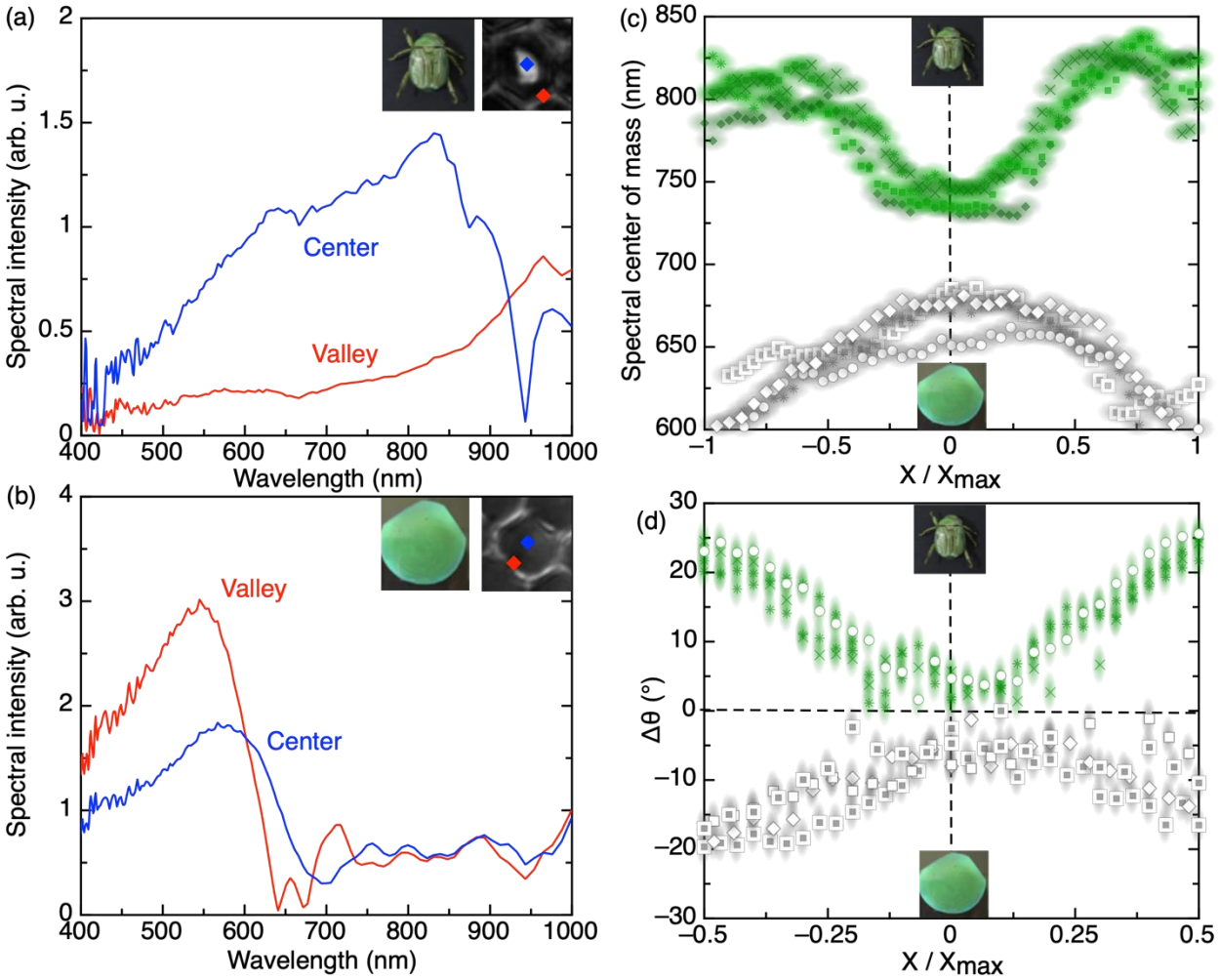

Figure 5: Typical spectral reflectivity for the center of a polygon (blue) and a valley (red) for (a) the biological sample and (b) synthetic sample PG30. The spectra are normalized with respect to

the lamp spectrum. (c) Spectral center of mass as a function of a normalized spatial coordinate for both samples (green: beetle, gray: PG30, the clouds represent the data error (±3nm). (d) Retrieved variation in the helical axis orientation for both samples as a function of a normalized spatial coordinate (green: beetle, gray: PG30, the clouds represent the data error (±2°)).

We note a narrow overlap of the reflected spectral bandwidths, and for both regions (center and valley), the maximal intensity occurs at opposite regions of the spectrum, at high (resp. low) wavelength for the biological (resp. synthetic) sample. This is a consequence of the opposite curvatures of the stripes in the fingerprint texture: concave in the biological sample (Fig. 1e) and convex in the synthetic sample (Fig. 2c). Such a difference may lead to a convergent or divergent mirror with wavelength-sensitive behavior. For the biological sample, as already seen with the hyperspectral cubes, the center of the polygon exhibits a broad reflectivity covering most of the visible part of the spectrum, while valleys have a lower but constant contribution, which increases above 800 nm (Fig. 5a). In the valleys, the orientation of the stripes in the fingerprint texture is perpendicular to the normal to the material surface (Figs. 1e and Fig. 2c), which means that in both materials, the helix orientation is not tilted in these narrow regions between polygonal cells. The synthetic sample (Fig. 5b) has a maximum reflectivity at approximately 530 nm for the valley and approximately 580 nm for the center, both followed by a sharp spectral cutoff at approximately 650-700 nm. The incoming light is barely reflected for higher wavelengths.

In a former study[43] on synthetic polygonal textures, we proposed quantifying the twisted structure at the scale of a single polygonal cell by tracking the spatial dependence of the spectral center of mass, defined as:

$$\lambda_0 = \frac{\int \lambda I(\lambda) d\lambda}{\int I(\lambda) d\lambda} \quad (1)$$

As already mentioned in the first section, the pattern arises from a repeated twisted structure in which the orientation of the helical axis slightly changes in the lateral part of a polygon. The spatially varying orientation of the helical axis is accompanied by light-shaping properties and their spectral dependence.[41] In reflection, the orientation-changing twist is associated with a change of the Bragg band following $\lambda_0 = n\, p\, cos(\theta)$, where n is the average refractive index of the material, p is the pitch of the helix and θ is the angle between the helical axis and the direction of the incident light. Therefore, the HSI measurement of the transverse modulation of the central reflected wavelength enables us to directly picture the local tilt of the helical axis.

The center of mass is then calculated for the two samples considering the overall spectral bandwidth (400 nm—1000 nm), as a function of a transverse normalized coordinate ($X/X_{max}=0$ for the center of a polygon, $X/X_{max}=1$ for a valley). The results are shown in Fig. 5c for four different hexagonal cells. The chromatic features of the biological sample are found to be nicely reproducible from one microcell to another. A first comparative result arises from the observation that the two curves are completely disjointed. This perfectly illustrates the gap between the chiro-optical properties of the bioinspired and biological samples, which would have to be especially taken into consideration to design a so-called biomimetic material. Furthermore, the spectral-spatial dependences are curved in opposite directions. For the biological sample, a plateau around the microcell center is followed by a sharp redshift of the center of mass from the center to the valleys. For PG30, the trend is smoother, but the center of mass is clearly shifted towards shorter wavelengths (blueshift) from the center to the valleys. The opposite spectral shifts indicate a change in the sign of the curvature of the helical axis tilting. As shown in Fig. 5d, the variation of

the curvature of the helical axis from the center to the valleys is found to be positive (resp. concave) for the biological green band and negative (resp. convex) for the synthetic film. The maximum absolute tilt is close to 20° for the latter and up to 30° for the former.

To conclude this section, the analysis has revealed two major structural differences: concave versus convex arrangement of the stripes in the fingerprint texture and the influence of the pitch-gradient structure on the width of the reflection bandwidth. In the following, we aim to investigate in synthetic textures the use of the sample thickness as a way to reveal the influence of the propagation of the curvature of cholesteric pseudo-layers in relation to the spatial confinement of this propagation.

3.2 Tuning the optical behavior via the thickness of synthetic films

We present here the hyperspectral analysis of four different PGd samples, characterized by four different thicknesses, as summarized in Table 1, where d is the film thickness. The thickness influences the polygon size[42] and the extension of the arc patterns in the bulk of the film. For a given annealing time, there exists a threshold thickness above which the arc patterns do not propagate to the bottom of the film, close to the substrate. In this region, the fingerprint texture is free of arcs and exhibits straight stripes.

The results are presented as hyperspectral cubes (Fig. 6). Again, the samples are presented in two spatial dimensions and one spectral dimension, the latter being reduced to the maximal reflectivity bandwidth (400 nm—700 nm). The cubes show a qualitatively reproducible spatial-chromatic distribution: most of the reflected light is between 450 nm and 650 nm, with a sharp cutoff at approximately 650 nm and a bright contribution of edges and valleys. One can note the filament texture in PG6. It should also be emphasized that the contribution of the valleys is

more spatially localized when the film is thinner, which indicates that the nested arcs have not propagated over the entire thickness for the thickest films.

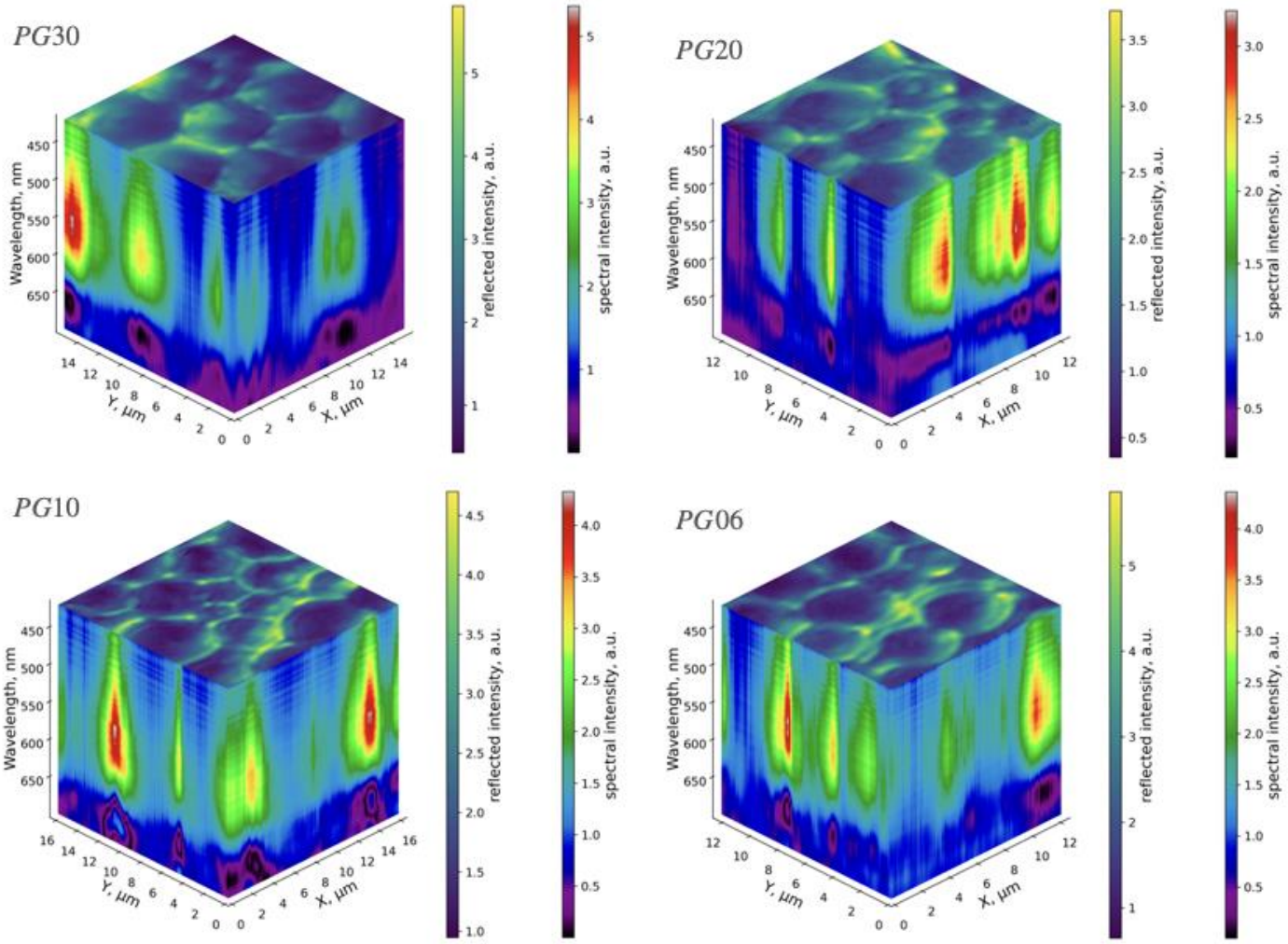

Figure 6: Hyperspectral datacubes for the PG30, PG20, PG10, and PG06 films, with thicknesses of 30 µm, 20 µm, 10 µm and 06 µm, respectively. Two different color bars are associated with each cube. The black-to-yellow color bar refers to the overall reflected intensity (i.e., not spectrally resolved), as plotted on the top of the cube (*X* versus *Y*) The second color bar (black-to-red) refers

to the reflected spectral intensity, as plotted on the cube sides (wavelength versus *X*, wavelength versus *Y*).

The variation of the local tilt of the helical axis across one polygon is determined following the procedure described in the former section. The θ spatial dependence as a function of a normalized transverse coordinate is shown in Fig. 7. Again, the overall trend is nicely reproduced from one sample to another. However, the thinnest films exhibit a larger maximum tilt, which agrees with the propagation of the nested arc structure throughout the full thickness.

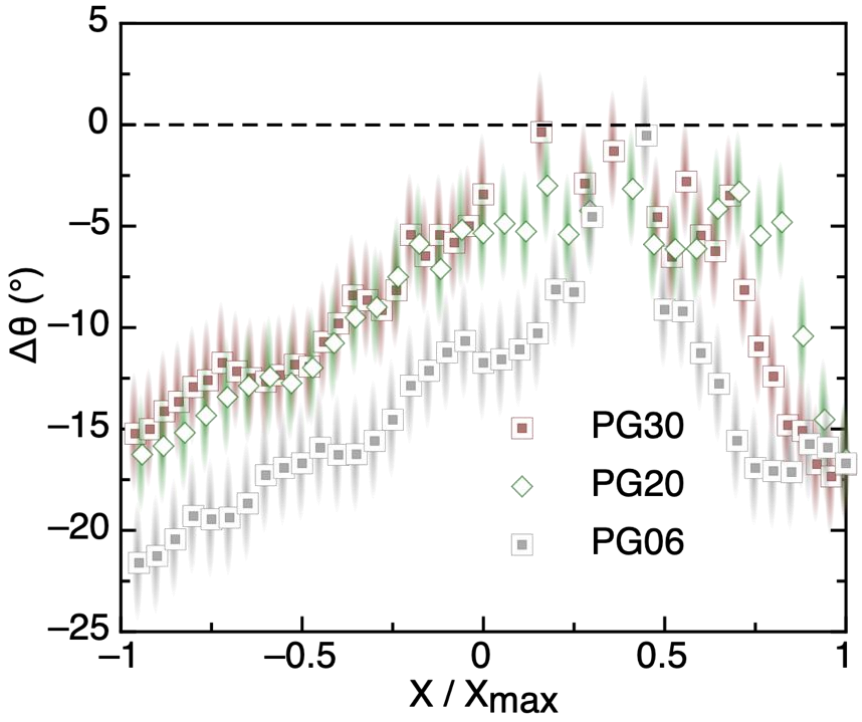

Figure 7: Retrieved variation in the helical axis orientation for three samples as a function of a normalized spatial coordinate. The clouds represent the data error (±2°).

4 Conclusions

In the field of biomimicry, we used hyperspectral imaging to compare, within a common methodology, the optical behaviors of an array of reflective microcells with a complex twisted organization of constituents, i.e., chitin fibers in the biological sample and oligomer molecules in the artificial sample. The twisted organization consists of a cholesteric liquid crystal structure that associates fixed and spatially varying orientations of the helical axis and a graded pitch versus a constant pitch. The main similarities and differences can be summarized as follows:

- Common features: similar polygonal patterns according to optical microscopy. The polygonal microcells act as wavelength-selective micromirrors; i.e., the light intensity is differently distributed in the different parts of the microcell (center, lateral part, and valley between cells). The fingerprint textures in transverse sections exhibit arc patterns in the upper part and straight stripes in the lowest part, which corresponds to a mix of tilted and fixed orientations of the helical axis. The tilt angle ranges are close (up to ~25° in the biological microcell vs ~20° in the synthetic one).
- Divergent features: concave (resp. convex) structures in the biological (resp. synthetic) material; opposite distributions of the spectral center of mass between 600 nm and 850 nm with a symmetry axis at 700 nm, related to the opposite concavities; graded (constant) helical pitch in the biological (synthetic) material; broad (narrow) reflection between 500 nm and 1000 nm in the cuticle (synthetic film) as a consequence of the previous structural feature; a bright central spot (bright valley) in the biological (synthetic) material over a broad wavelength band, i.e., 440 nm-950 nm (no bright spot in the synthetic samples, but the

polygon center is alternately bright or dark depending on the wavelength); and narrow overlap of the reflected spectral bandwidths for a single cell.

Additionally, varying the thickness of the synthetic films offers the possibility to tune the tilt angle of the helical axis inside a microcell, which can thus offer variable spatial modulation of the reflected light.

By shedding light on the common features and differences in the physical properties of polygonal textures, this study constitutes a preliminary approach to defining the specifications of a biomimetic fabrication procedure aiming at producing novel optical components. Numerous applications may derive from insect cuticle patterning,[56] like color control (e.g.: tuning color, increasing—or reducing—reflectance or scattering or absorbance), light emission optimization, microdevices (e.g.: lenses, mirrors), solar cells, anti-counterfeit labels, photonic integrated circuits—to limit this short list to the field of optics. The twisted CLC patterns issued from the present microcells may inspire practical uses in micro-optics and nanophotonics, in the field of non-specular properties such as deflection and lensing in geometric phase planar optics.[57-59] The phase of light that is Bragg-reflected off the helical structure can be controlled over 0–2π depending on the spatial phase of the helical structure.[57] The manufacture of planar elements with arbitrary reflected wave fronts via orientation control is thus desired. This requires the helix phase to vary depending on position, which objective is reached with chiral tessellations like those under this investigation.

Data accessibility. Relevant experimental data are available at https://doi.org/10.5061/dryad.ttdz08kv4 [61].

Authors' contributions. A. S. carried out the manufacture of synthetic films. M. M. prepared the biological samples, supervised the work of acquiring TEM and AFM images of biological and synthetic samples. M. N. and A.J. built the hyperspectral microscope, acquired and analysed the data. A. J. and M. M. led the conceptual development of the research and wrote the manuscript. All authors gave final approval for publication and agree to be held accountable for the work performed therein.

Competing interests. The authors declare no competing interest.

Funding. This work was supported by the Agence Nationale de la Recherche (France) under grant number ANR-17-CE30-0025.

Acknowledgements. M. M. thanks Dr. E. Hanelt from Wacker Chemie GmbH (Munchen, Germany) for providing him with oligomers, Ms. V. Soldan (METi, CBI, CNRS, University of Toulouse) for her technical assistance with ultramicrotomy and TEM observations of biological sample (Fig. 1e), Dr. G. Seine for AFM imaging (Fig. 2b) and Mr. C. Bourgerette for his technical assistance with ultramicrotomy and TEM observations of synthetic sample (Fig. 2c).

References

[1] P. Ball, *The Self-Made Tapestry-Pattern formation in nature*, Oxford University Press, **1999**.

[2] D. Lee, *Nature's Palette-The Science of Plant Color*, The University of Chicago Press, **2007.**

[3] M. Kolle, S. Lee, *Progress and Opportunities in Soft Photonics and Biologically Inspired Optics*, Adv. Mater. **2018**, *30*, 1702669

[4] Y. Yang, X. Song, X. Li, Z. Chen, C. Zhou, Q. Zhou, Y. Chen, *Recent Progress in Biomimetic Additive Manufacturing Technology: From Materials to Functional Structures*, Adv. Mater. **2018**, *30*, 1706539.

[5] U. G. K. Wegst, H. Bai, E. Saiz, A. P. Tomsia, R. O. Ritchie, *Bioinspired structural materials*, Nat. Mater. **2015**, *14*, 23.

[6] A. E. Filippov, A. Kovalev, S. N. Gorb, *Numerical simulation of the pattern formation of the springtail cuticle nanostructures*, J. R. Soc. Interface **2018**, *15*, 20180217.

[7] T. Lenau, M. Barfoed, *Colours and Metallic Sheen in Beetle Shells*, Adv. Eng. Mat. **2008**, *10*, 299.

[8] M. Mitov, *Cholesteric liquid crystals in living matter*, Soft Matter **2017**, *13*, 4176.

[9] Y. Bouligand, C. R. Acad. Sci. Hebd. Seances Acad. Sci. D **1965**, *261*, 4864.

[10] P.-G.deGennes, J.Prost, *Cholesterics in The Physics of Liquid Crystals* - 2nd edn, Ch.6, Oxford University Press, Oxford, **1993**.

[11] E. Snell-Rood, *Bring biologists into biomimetics*, Nature **2016**, *529*, 277.

[12] N. Kaiser and H. K. Pulker, *Optical Interference Coatings*, Springer, New York, USA **2003**.

[13] Y. Zhu, W. Zhang and D. Zhang, *Fabrication of Sensor Materials Inspired by Butterfly Wings*, Adv. Mater. Technol. **2017**, *2*, 160020.

[14] J. Hasan, A. Roy, K. Chatterjee and P. K. V. D Yarlagadda, *Mimicking Insect Wings: The Roadmap to Bioinspiration*, ACS Biomater. Sci. Eng. **2019**, *5*, 3139−3160.

[15] A. Matranga, S. Baig, J. Boland, C. Newton, T. Taphouse, G. Wells and S. Kitson, *Biomimetic Reflectors Fabricated Using Self-Organising, Self-Aligning Liquid Crystal Polymers*, Adv. Mater. **2013**, *25*, 520.

[16] S. N. Fernandes, P. L. Almeida, N. Monge, L. E. Aguirre, D. Reis, C. L. P. de Oliveira, A. M. F. Neto, P. Pieranski and M. H. Godinho, *Mind the Microgap in Iridescent Cellulose Nanocrystal Films*, Adv. Mater. **2017**, *29*, 1603560.

[17] L. de Silva, I. Hodkinson, P. Murray, Q.H. Wu, M. Arnold, J. Leader, A. McNaughton, *Natural and nanoengineered chiral reflectors: structural color of manuka beetles and titania coatings*, Electro- magnetics **2005**, *25*, 391.

[18] K. Buhl, Z. Roth, P. Srinivasan, R. Rumpf, E. Johnson, *Biologically inspired optics: analog semiconductor model of the beetle exoskeleton*, Proc. SPIE **2008**, *7057*, 1.

[19] S.A. Jewell, P. Vukusic, N.W. Roberts, *Circularly polarized colour reflection from helicoidal structures in the beetle Plusiotis boucardi*, N. J. Phys. **2007**, *9*, 1

[20] F. Liu, H. Yin, B. Dong, Y. Qing, L. Zhao, S. Meyer, X. Liu, J. Zi, B. Chen, *Inconspicuous structural coloration in the elytra of beetles Chlorophila obscuripennis (Coleoptera)*, Phys. Rev. E **2008**, *77*, 012901.

[21] A.E. Seago, P. Brady, J.-P. Vigneron, T.D. Schultz, *Gold bugs and beyond: a review of iridescence and structural colour mechanisms in beetles (Coleoptera)*, J. R. Soc. Interface **2008**, 5, S165.

[22] T.D. Schultz, M.A. Rankin, *The ultrastructure of the epicuticular interference reflectors of tiger beetles (Cicindela)*, J. Exp. Biol. **1985**, *117*, 87.

[23] J.P. Vigneron, M. Ouedraogo, J.-F. Colomer, M. Rassart, *Spectral sideband produced by a hemispherical concave multilayer on the African shield-bug Calidea panaethiopica (Scutelleridae)*, Phys. Rev. E **2009**, *79*, 021907.

[24] D.K. Stavenga, B.D. Wilts, H.L. Leertouwer, T. Hariyama, *Polarized iridescence of the multilayered elytra of the Japanese jewel beetle Chrysochroa fulgidissima*, Phil. Trans. B **2011**, *366*, 709.

[25] D.Wilts, H.M. Whitney, B.J. Glover, U. Steiner, S. Vignolini, *Natural helicoidal structures: morphology, self-assembly and optical properties*, Mater. Today Proc. **2014**, *1S*, 177.

[26] M. Hernandez-Jimenez, D.E. Azofeifa, E. Libby, C. Barboza-Aguilar, A. Solis, L. Arce-Marenco, I. Garcia-Aguilar, A. Hernandez, W.E. Vargas, *Qualitative correlation between structural chirality through the cuticle of Chrysina aurigans scarabs and left-handed circular polarization of the reflected light*, Opt. Mater. Express **2014**, *4*, 2632.

[27] L. Fernandez del Rio, H. Arwin, K. Jarrendahl, *Polarizing properties and structure of the cuticle of scarab beetles from the Chrysina genus*, Phys. Rev. E **2016**, *94*, 012409.

[28] G. Agez, C. Bayon, M. Mitov, *Multiwavelength micromirrors in the cuticle of scarab beetle Chrysina gloriosa*, Acta Biomater. **2017**, *48*, 357.

[29] G. J. Blomquist, A.-G. Bagnères, *Insect Hydrocarbons-Biology, Biochemistry and Chemical Ecology*, Cambridge University Press, Cambridge, **2010**.

[30] M. Mitov, V. Soldan, S. Balor, Arthropod Struct. and Development **2018**, *47*, 622.

[31] A. Pace, *Cholesteric liquid crystal-like structure of the cuticle of Plusiotis gloriosa*, Science **1972**, *176*, 678

[32] V. Sharma, M. Crne, J. O. Park, M. Srinivasarao, *Structural origin of circularly polarized iridescence in jeweled beetles*, Science **2009**, *325*, 449.

[33] L. Fernandez del Rio, H. Arwin, K. Järrendahl, *Polarizing properties and structural characteristics of the cuticle of the scarab beetle Chrysina gloriosa*, Thin Solid Films **2014**, *571*, 410

[34] P. Bouchal, J. Kapitan, M. Konecny, M. Zboncak and Z. Bouchal, *Non-diffracting light in nature: Anomalously reflected self-healing Bessel beams from jewel scarabs*, APL Photon. **2019**, *4*, 126102

[35] R. Meister, H. Dumoulin, M.-A. Halle and P. Pieranski, J. Phys. II France **1996**, *6*, 827-844.

[36] R. Meister, M.-A. Halle, H. Dumoulin and P. Pieranski, Phys. Rev E. **1996**, *54*, 3771-3782.

[37] G. Agez, R. Bitar and M. Mitov, *Color selectivity lent to a cholesteric liquid crystal by monitoring interface-induced deformations,* Soft Matter **2011**, *7*, 2841.

[38] A. Bobrovsky, K. Mochalov, A. Chistyakov, V. Oleinikov, and V. Shibaev, *Features of Double-Spiral Valley-Hills Surface Topography Formation in Photochromic Cholesteric Oligomer-Based Films and Their Changes Under Polarized Light Action*, Macromol. Chem. Phys. **2012**, *213*, 2639.

[39] A. Bobrovsky, O. Sinitsyna, A. Abramchuk, I. Yaminsky, and V. Shibaev, *Atomic force microscopy study of surface topography of films of cholesteric oligomer- and polymer-based mixtures with photovariable helix pitch*, Phys. Rev. E **2013** *87*, 012503.

[40] O. Sinitsyna, A. Bobrovsky, I. Yaminsky, and V. Shibaev, Colloid Polym. Sci. **2014**, *292*, 1567.

[41] C. Bayon, G. Agez and M. Mitov, *Wavelength-tunable light shaping with cholesteric liquid crystal microlenses,* Lab on a Chip **2014**, *14*, 2063.

[42] C. Bayon, G. Agez and M. Mitov, *Size-effect of oligomeric cholesteric liquid-crystal microlenses on the optical specifications*, Opt. Lett. **2015**, *40*, 4763.

[43] A. Jullien, A. Scarangella, U. Bortolozzo, S. Residori and M. Mitov, *Nanoscale hyperspectral imaging of of cholesteric liquid crystals with oblique helicticity*, Soft Matter **2019**, *15*, 3256.

[44] Y. Bouligand, *Recherches sur les textures des états mésomorphes: Les champ polygonaux dans les cholestériques*, J. Phys. **1972**, *33* 715.

[45] A. Saupe, *Disclinations and Properties of the Director field in Nematic and Cholesteric Liquid Crystals*, Mol. Cryst. Liq. Cryst. **1973**, *21*, 211-238.

[46] F. H. Kreuzer, N. Haberle, H. Leigeber, R. Maurer, J. Stohrer and J. Weis, *Organo-silicon Chemistry Set*, eds. N. Auner and J. Weis, in Organosilicon Chemistry Set, eds. N. Auner and J. Weis, Wiley-VCH Verlag GmbH, **2005**.

[47] D. C. Zografopoulos, E. E. Kriezis, M. Mitov, and C. Binet, *Theoretical and experimental studies of hyper-reflective polymer-network cholesteric liquid crystal structures with helicity inversion*, Phys. Rev. E **2006**, *73*, 061701.

[48] K. H. Yang, *Measurements of empty cell gap for liquid-crystal displays using interferometric methods*, J. App. Phys. **1988**, *64*, 4780.

[49] A. Jullien, R. Pascal, U. Bortolozzo,N. Forget and S. Residori, *Liquid-crystal based Fourier-transform spectrometer applied to high-resolution hyperspectral imaging*, Optica **2017**, *4*, 400

[50] Z. Dabiri and S. Lang ISPRS Int. J. Geo-Inf. **2018**, *7*, 488.

[51] H. F. Grahn and P. Geladi, *Techniques and applications of hyperspectral analysis*, Wiley **2007**.

[52] P. R. Griffiths and J. A. de Haseth, *Fourier Transform Infrared Spectrometry*, Wiley **2007**.

[53] A. Boniface, I. Gusachenko, K. Dholakia and S. Gigan, *Rapid broadband characterization of scattering medium using hyperspectral imaging*, Optica **2019**, *6*, 274-279

[54] A. Candeo, B. E. Nogueira de Faria, M. Erreni, G. Valentini, A. Bassi, A. M. de Paula, G.

Cerullo, C. Manzoni, *A hyperspectral microscope based on an ultrastable common-path interferometer*, APL photonics **2019**, *4*, 120802

[55] C. Carrizo, A. Gilerson, R. Foster, A. Golovin and A. El-Habashi, *Characterization of radiance from the ocean surface by hyperspectral imaging*, Opt. Express **2019**, *27*, 1750- 1768

[56] G. S. Watson, J. A. Watson and B. W. Cribb, *Diversity of Cuticular Micro- and Nanostructures on Insects: Properties, Functions, and Potential Applications*, Annu. Rev. Entomol. **2017**, *62*, 185-205.

[57] J. Kobashi, H. Yoshida, and M. Ozaki, *Planar optics with patterned chiral liquid crystals*, Nat. Photon. **2016** *10*, 389-392.

[58] P. Chen, L. L. Ma, W. Hu, Z. H. Shen, H. K. Bisoyi, S. B. Wu, S. J. Ge, Q. Li, Y. Q. Lu, *Chirality invertible superstructure mediated active planar optics*, Nat. Commun. **2019**, *10*, 2518.

[59] L. L. Ma, W. Hu, Z. G. Zheng, S. B. Wu, P. Chen, Q. Li, Y. Q. Lu, *Light-Activated Liquid Crystalline Hierarchical Architecture Toward Photonics*, Adv. Optical Mater. **2019**, 1900393.

[60] Y. Zhang, O. Paris, N.J. Terrill, H. S. Gupta, *Uncovering three-dimensional gradients in fibrillar orientation in an impact-resistant biological armour*, Sci. Rep. **2016**, *6*, 26249.

[61] A. Jullien, M. Neradovskiy, A. Scarangella, M. Mitov M. 2020 Data from: Biomimicry of iridescent, patterned insect cuticles: comparison of biological and synthetic, cholesteric microcells using hyperspectral imaging. Dryad Digital Repository. (https://doi.org/10.5061/dryad.ttdz08kv4)